Special Article - Tools for Experiment and Theory

Elastic $\pi^+ p$ and $\pi^+\pi^+$ scattering at LHC

A.E. Sobol[1,a], **R.A. Ryutin**[1,b], **V.A. Petrov**[1,c], **M.J. Murray**[2,d]

[1]Institute for High Energy Physics, 142 281, Protvino, Russia
[2]University of Kansas, Lawrence, USA

Abstract We discuss the possibility of measuring leading neutron production at the LHC. These data could be used to extract from it $\pi^+ p$ and $\pi^+\pi^+$ cross sections. In this note we give some estimates for the case of elastic cross sections and discuss related problems and prospects.

1 Introduction

In a recent paper [1] we pushed forward the idea of using the Zero Degree Calorimeters, ZDCs, designed for different uses at several of the LHC collaborations, to extract the total cross section of the processes $\pi p \to X$ and $\pi\pi \to X$ at energies about 1–5 TeV. This would allow us to use the LHC as a πp and $\pi\pi$ collider. In [1] there was also mentioned possible measurements of the elastic πp and $\pi\pi$ scattering. The physics motivation for extending this program to elastic scattering is very clear since the total and elastic cross sections are so tightly interrelated (e.g., via unitarity) that any testing of various models of high-energy hadron interactions is of little informative use without both of them (Fig. 1).

We would like also to remind to the reader an idea of *universality of strong interactions* at superhigh energies, in the sense that any ratio of two total or elastic cross sections will asymptotically approach 1 independently of initial states (Fig. 2a). How close we are to reaching the asymptotic regime, *asymptopia*, can be tested when looking at the ratio of elastic to total cross sections. Most of theories predict it to be 1/2 [2–6] (Fig. 2b), though there are some theories which predict it to be equal to 1 [9, 10] (Fig. 2c). Sure, this can and will be done. The TOTEM experiment has been designed to

measure this ratio but any information about such a feature for the interaction of the *lightest hadrons* is impossible to overestimate.

There are many other questions to be asked. For instance, how different are the interaction radii in pp, πp and $\pi\pi$ high-energy collisions? The properties of the interaction region could be obtained from diffractive patterns, which are different for these processes at the same energy (Fig. 3). It would be interesting to know the dependence of these interactions on the very different quark–gluon content of colliding particles etc. If it will be possible to provide such a marvellous opportunity as access to the data on πp and $\pi\pi$ TeV-energy interactions all the landscape of the "soft physics" will be transformed to the better. In what follows we present our estimates on the possibility to extract πp and $\pi\pi$ elastic cross sections using CMS as an example. Just before sending this article to arxiv a paper on the four-body reaction $pp \to nn\pi^+\pi^+$ at the LHC was placed there. However, the authors of [11] do not estimate possibilities for extraction of the $\pi\pi$ elastic cross section.

2 Exclusive single-pion exchange

The diagram of the exclusive single-pion exchange (SπE) process $p + p \to n + \pi^+ + p$ is presented in Fig. 4a. The momenta are p_1, p_2, p_n, p'_π, p'_2 respectively. In the center-of-mass frame these can be represented as follows (boldface letters denote transverse momenta):

$$p_i \simeq \left(\frac{\sqrt{s}}{2}, (-1)^{i-1}\frac{\sqrt{s}}{2}, \mathbf{0} \right), \tag{1}$$

$$p_n \simeq \left((1-\xi)\frac{\sqrt{s}}{2}, (1-\xi)\frac{\sqrt{s}}{2}, -\boldsymbol{q} \right), \tag{2}$$

$$p'_2 \simeq \left((1-\xi_p)\frac{\sqrt{s}}{2}, -(1-\xi_p)\frac{\sqrt{s}}{2}, \boldsymbol{q} - \boldsymbol{k} \right), \tag{3}$$

[a] e-mail: Andrei.Sobol@cern.ch

[b] e-mail: Roman.Rioutine@cern.ch

[c] e-mail: Vladimir.Petrov@cern.ch

[d] e-mail: mjmurray@ku.edu

642

Eur. Phys. J. C (2010) 69: 641–655

Fig. 1 (**a**) Total pp cross sections in the energy range $0.5\,\text{TeV} < \sqrt{s} < 15\,\text{TeV}$ for parametrizations [2] (*solid*), [3] (*dashed*), [4] (*dotted*) and [5, 6] (*dash-dotted*). Data points are taken from [7]; (**b**) evolution of the diffractive pattern in the pp scattering for $\sqrt{s} = 1 \to 20\,\text{TeV}$ (from *right* to *left*) for parametrizations from [4] (*solid*) and [8] (*dashed*)
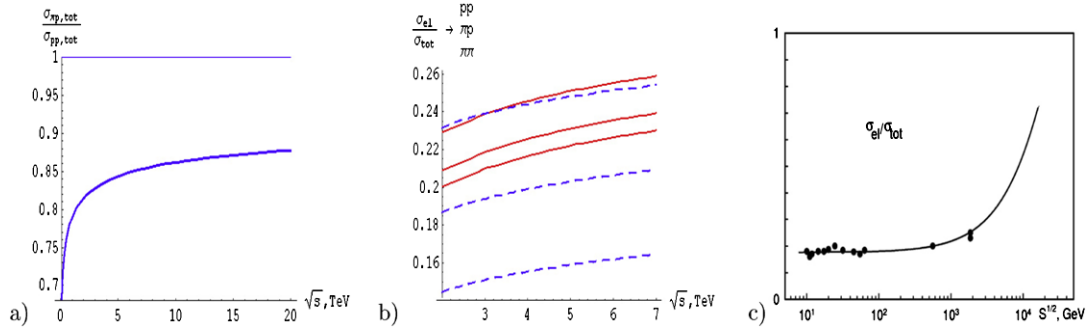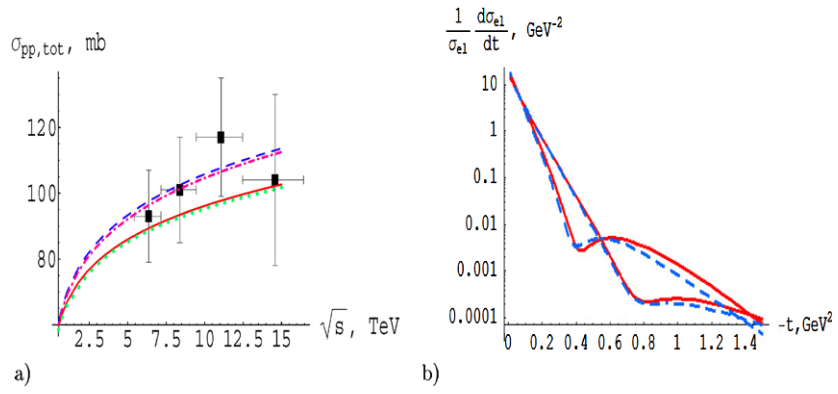

Fig. 2 (**a**) Ratio of $\pi^+ p$ to pp total cross sections for COMPETE [3] parametrization; (**b**) ratio of elastic to total cross sections for pp, $\pi^+ p$ and $\pi^+ \pi^+$ processes for parametrizations [4] (*solid*) and [5, 6] (*dashed*); (**c**) ratio of proton–proton elastic to total cross sections in [9, 10]

Fig. 3 Evolution of diffractive pattern for pp (*solid*), $\pi^+ p$ (*dashed*) and $\pi^+ \pi^+$ (*dotted*) elastic processes at (**a**) $\sqrt{s} = 5\,\text{TeV}$ and (**b**) $\sqrt{s} = 14\,\text{TeV}$ for the parametrization from the Appendix B
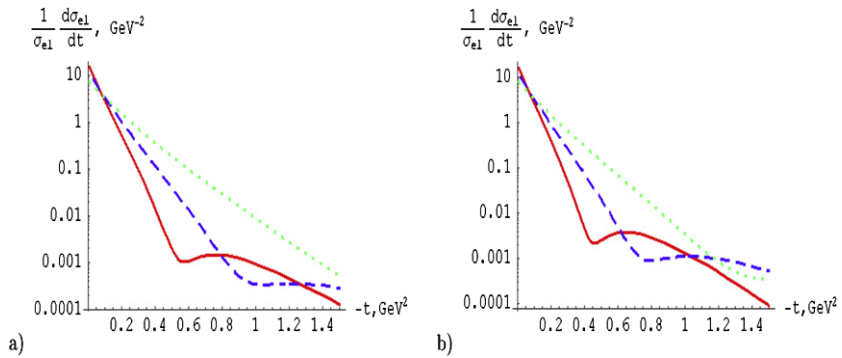
$$p_\pi = p_1 - p_n, \qquad p'_\pi = p_2 + p_\pi - p'_2, \tag{4}$$

$$M^2 = (p_\pi + p_2)^2 = (p'_\pi + p'_2)^2, \tag{5}$$

$$\xi \simeq \frac{M^2}{s}, \qquad \xi_p \simeq \frac{m_\pi^2 + k^2}{\xi s}, \tag{6}$$

$$t = (p_1 - p_n)^2 = p_\pi^2 \simeq -\frac{q^2 + \xi^2 m_p^2}{1 - \xi}, \tag{7}$$

$$t_p = (p_2 - p'_2)^2 \simeq -\frac{(q - k)^2 + \xi_p^2 m_p^2}{1 - \xi_p}. \tag{8}$$

As an approximation for π exchange we use the formula shown graphically in Fig. 5a. If we take into account absorptive corrections this formula can be rewritten as

$$\frac{d\sigma_{X,\text{S}\pi\text{E}}}{d\xi \, dt \, d\Phi_X} = \frac{G_{\pi^+ pn}^2}{16\pi^2} \frac{-t}{(t - m_\pi^2)^2} F^2(t) \xi^{1 - 2\alpha_\pi(t)}$$

$$\times \frac{d\sigma_{X,\pi^+ p}(\xi s)}{d\Phi_X} S(s/s_0, \xi, t), \tag{9}$$

where Φ_X is the phase space for the system X produced in the $\pi^+ p$ scattering, the pion trajectory is $\alpha_\pi(t) = \alpha'_\pi(t - m_\pi^2)$. The slope $\alpha' \simeq 0.9\,\text{GeV}^{-2}$, $\xi = 1 - x_L$,
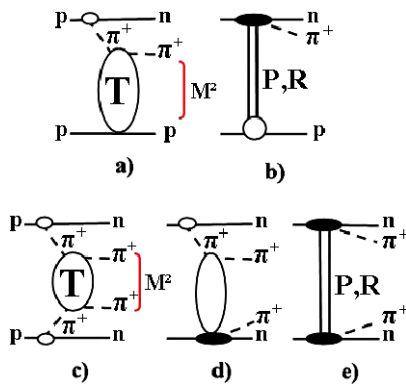
Fig. 4 Diagrams for the exclusive signal and background processes in leading neutrons production (initial rescattering corrections are not shown). (**a**) Signal for the elastic $\pi^+ p$ scattering: process with an exclusive single-pion exchange (SπE) $p + p \to n + \pi^+ + p$, M is the mass of the $\pi^+ p$ system; (**b**) background for the elastic $\pi^+ p$ scattering: low mass single dissociation with pomeron and reggeon exchanges; (**c**) signal for the elastic $\pi^+ \pi^+$ scattering: process with an exclusive double pion exchange (DπE) $p + p \to n + \pi^+ + \pi^+ + n$, M is the mass of the $\pi^+ \pi^+$ system; (**d**) background for the elastic $\pi^+ \pi^+$ scattering: SπE with single low mass dissociation in the $\pi^+ p$ channel; (**e**) background for the elastic $\pi^+ \pi^+$ scattering: low mass double dissociation with pomeron and reggeon exchanges
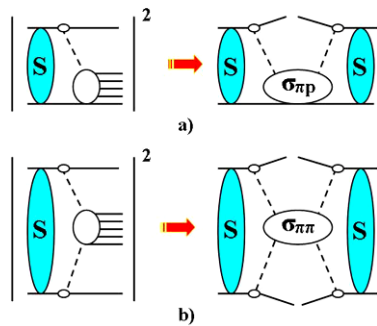

Fig. 5 Amplitudes squared and cross sections of the processes: (**a**) $p + p \to n + X$ (SπE), (**b**) $p + p \to n + X + n$ (DπE). S represents soft rescattering corrections. In this note $X = \pi^+ + p$ (elastic SπE) and $X = \pi^+ + \pi^+$ (elastic DπE)

were x_L is the fraction of the initial proton's longitudinal momentum carried by the neutron, and $G^2_{\pi^0 pp}/(4\pi) = G^2_{\pi^+ pn}/(8\pi) = 13.75$ [12, 13]. The form factor $F(t)$ is usually expressed as an exponential:

$$F(t) = \exp(bt), \tag{10}$$

where, from recent data [14, 15], we expect $b \simeq 0.3$ GeV^{-2}. We are interested in the kinematical range

$$0.01 \text{ GeV}^2 < |t| < 0.5 \text{ GeV}^2, \qquad \xi < 0.4, \tag{11}$$

where formula (9) dominates according to [16] and [17]. At high energies we can use any adequate parametrizations of different $\pi^+ p$ cross sections. Here we replace

$d\sigma_{X,\pi^+ p}/d\Phi_X$ in (9) by $d\sigma_{\text{el},\pi^+ p}/dt_p$ (or integrated $\sigma_{\text{el},\pi^+ p}$) instead of $\sigma_{\text{tot},\pi^+ p}$ in [1].

The suppression factor S arises from absorptive corrections [18]. We estimate absorption in the initial state for inclusive reactions and for both initial and final states in exclusive exchanges. For this task we use our model with three pomeron trajectories [8]:

$$\alpha_{\text{IP}_1}(t) - 1$$
$$= (0.0578 \pm 0.002) + (0.5596 \pm 0.0078)t,$$

$$\alpha_{\text{IP}_2}(t) - 1$$
$$= (0.1669 \pm 0.0012) + (0.2733 \pm 0.0056)t, \tag{12}$$

$$\alpha_{\text{IP}_3}(t) - 1$$
$$= (0.2032 \pm 0.0041) + (0.0937 \pm 0.0029)t.$$

These trajectories are the result of a 20 parameter fit of the total and differential cross sections in the region

$$0.01 \text{ GeV}^2 < |t| < 14 \text{ GeV}^2,$$

$$8 \text{ GeV} < \sqrt{s} < 1800 \text{ GeV}.$$

Although the $\chi^2/d.o.f. = 2.74$ is rather large, the model gives good predictions for the elastic scattering (especially in the low-t region with $\chi^2/d.o.f. \sim 1$).

We use the procedure described in [19, 20] to estimate the absorptive corrections. With an effective factorized form of the expression (13) used for convenience, we obtain

$$\frac{d\sigma_{\text{el},S\pi E}(s/s_0, \xi, \boldsymbol{q}^2)}{d\xi \, d\boldsymbol{q}^2 \, dt_p}$$

$$= (m_p^2 \xi^2 + \boldsymbol{q}^2) |\Phi_B(\xi, \boldsymbol{q}^2)|^2$$

$$\times \frac{\xi}{(1-\xi)^2} \frac{d\sigma_{\text{el},\pi^+ p}(\xi s)}{dt_p} S(s/s_0, \xi, \boldsymbol{q}^2), \tag{13}$$

$$S = \frac{m_p^2 \xi^2 |\Phi_0(s/s_0, \xi, \boldsymbol{q}^2)|^2 + \boldsymbol{q}^2 |\Phi_s(s/s_0, \xi, \boldsymbol{q}^2)|^2}{(m_p^2 \xi^2 + \boldsymbol{q}^2) |\Phi_B(\xi, \boldsymbol{q}^2)|^2}. \tag{14}$$

The functions Φ_0 and Φ_s arise from different spin contributions to the amplitude

$$A_{p\to n} = \frac{1}{\sqrt{1-\xi}} \bar{\Psi}_n (m_p \xi \hat{\sigma}_3 \cdot \Phi_0 + \boldsymbol{q}\hat{\sigma} \cdot \Phi_s) \Psi_p \tag{15}$$

and both are equal to Φ_B in the Born approximation. Here $\hat{\sigma}_i$ are Pauli matrices and $\bar{\Psi}_n$, Ψ_p are neutron and proton spinors. Functions $\Phi_{0,s,B}$ are given in Appendix A. For the $\pi^+ p$ elastic cross sections we use parametrizations from [4] and [5, 6], which are described in Appendices B and C respectively.

The differential cross sections for the process $p + p \to n + \pi^+ + p$ at $\sqrt{s} = 10$ TeV are depicted in Fig. 6. The total

644

Eur. Phys. J. C (2010) 69: 641–655

Fig. 6 Integrated cross sections of the SπE process $p + p \to n + \pi^+ + p$ for parametrizations from Appendices B (*solid*) and C (*dashed*). (**a**) $\frac{d\sigma}{d\xi}$ (0.01 GeV^2 < |t| < 0.5 GeV^2); (**b**) $\frac{d\sigma}{dt}$, $10^{-3} < \xi < 0.3$

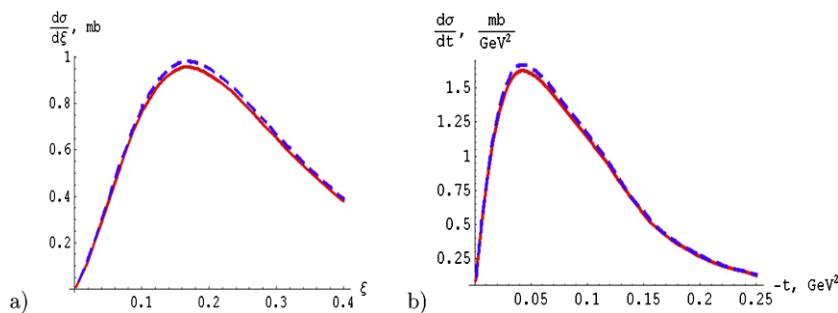**Table 1** Total $p + p \to n + \pi^+ + p$ cross sections in the kinematical region $0 < |q| < 0.5$ GeV, $\xi_{min} = 10^{-3} < \xi < \xi_{max}$ for two parametrizations given in Appendices B (C)

ξ_{max}	0.1	0.2	0.3	0.4
σ, µb	37.5 (39)	128 (132)	208 (214)	259 (266)

cross sections are listed in Table 1. They are in the range 8–270 µb for all values of $\xi_{max} < 0.4$ implying that we will have plenty of rate for the measurements.

At low energies ($\sqrt{s} < 70$ GeV) the region of applicability of our model is given by the inequalities (11). At higher energies this region may be smaller (say $\xi < 0.2$), since this corresponds to masses $M = 4.5$ TeV at $\sqrt{s} = 10$ TeV, and for larger masses the approach may break down.

3 Exclusive double pion exchange

As noted above, the Double pion Exchange (DπE) process can give information on both total and elastic $\pi\pi$ cross sections. $\pi\pi$ cross sections have been extracted in the past using the exclusive cross section [21]. The results are shown in Fig. 7. There is some tendency for an early flattening of the $\pi\pi$ cross sections. In πp and pp cross sections this flattening begins at higher energies and precedes further growth.

We can extend the analysis for one pion exchange described above to double pion exchange (Fig. 5b, DπE).

The kinematics of the exclusive DπE ($p + p \to n + \pi^+ + \pi^+ + n$, the momenta are p_1, p_2, p_{n_1}, p'_{π_1}, p'_{π_2}, p_{n_2} respectively) is similar to the exclusive double pomeron exchange process:

$$p_{\pi_i} \simeq \left(\xi_i \frac{\sqrt{s}}{2}, (-1)^{i-1} \xi_i \frac{\sqrt{s}}{2}, q_i \right),$$

$$p_{n_i} = p_i - p_{\pi_i}, \tag{16}$$

$$M^2 = (p_{\pi_1} + p_{\pi_2})^2 \simeq \xi_1 \xi_2 s - (q_1 + q_2)^2$$

$$\simeq \xi_1 \xi_2 s, \tag{17}$$

$$-t_i = \simeq \frac{q_i^2 + \xi_i^2 m_p^2}{1 - \xi_i}, \qquad t_{\pi\pi} = (p_{\pi_1} - p'_{\pi_1})^2. \tag{18}$$

The cross section can be evaluated as follows:

$$\frac{d\sigma_{X,D\pi E}}{d\xi_1 \, d\xi_2 \, dt_1 \, dt_2 \, d\Phi_X}$$

$$= \prod_{i=1}^{2} \left[\frac{G_{\pi^+ pn}^2}{16\pi^2} \frac{-t_i}{(t_i - m_\pi^2)^2} F^2(t_i) \xi_i^{1-2\alpha_\pi(t_i)} \right]$$

$$\times \frac{d\sigma_{X,\pi^+\pi^+}(\xi_1 \xi_2 s)}{d\Phi_X} S_2\big(s/s_0, \{\xi_i\}, \{t_i\} \big). \tag{19}$$

For the $\pi^+\pi^+$ elastic scattering we get

$$\frac{d\sigma_{el,D\pi E}(s/s_0, \{\xi_i\}, \{q_i^2\})}{d\xi_1 \, d\xi_2 \, dq_1^2 \, dq_2^2 \, dt_{\pi\pi}}$$

Fig. 7 Elastic and total cross sections for $\pi^-\pi^+$ and $\pi^-\pi^-$ scattering from the data on exclusive reactions as a function of the dipion invariant mass (Fig. 5 from [21])
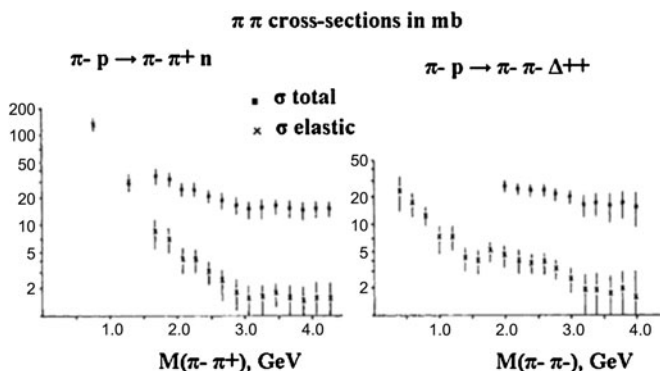
Fig. 8 Partially integrated cross sections of the $D\pi E$ process $p + p \to n + \pi^+ + \pi^+ + n$ at $\sqrt{s} = 10$ TeV for parametrizations from Appendices B (solid) and C (dashed): (a) $d\sigma/d\xi_1 d\xi_2$ for $\xi_1 = \xi_2 = \xi$ and $0 < |\boldsymbol{q}_{1,2}| < 0.5$ GeV; (b) $d\sigma/d\boldsymbol{q}_1^2 d\boldsymbol{q}_2^2$ for $|\boldsymbol{q}_1| = |\boldsymbol{q}_2| = |\boldsymbol{q}|$ and $10^{-3} < \xi_{1,2} < 0.3$
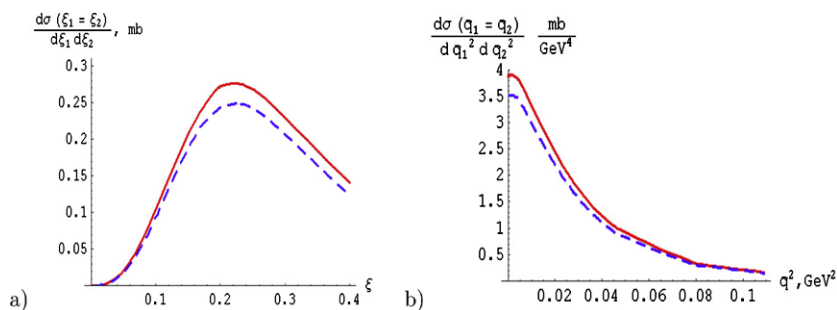

Table 2 Total $p + p \to n + \pi^+ + \pi^+ + n$ cross sections in the kinematical region $0 < |\boldsymbol{q}| < 0.5$ GeV, $\xi_{\min} = 10^{-3} < \xi < \xi_{\max}$ for two parametrizations from Appendices B (C)

$\xi_{\max}$	0.1	0.2	0.3	0.4
σ, µb	0.22 (0.19)	3.5 (3.1)	12 (11)	26.8 (24.7)

$$= \prod_{i=1}^{2}\left[\left(m_p^2\xi_i^2 + \boldsymbol{q}_i^2\right)\left|\Phi_B\left(\xi_i, \boldsymbol{q}_i^2\right)\right|^2 \frac{\xi_i}{(1-\xi_i)^2}\right]$$

$$\times S_2\left(s/s_0, \{\xi_i\}, \{\boldsymbol{q}_i^2\}\right)\frac{d\sigma_{\mathrm{el},\pi^+\pi^+}(\xi_1\xi_2 s)}{dt_{\pi\pi}}, \qquad (20)$$

$$S_2 = \frac{\sum_{i,j=0,s}\rho_{ij}^2|\bar{\Phi}_{ij}(s/s_0, \{\xi_i\}, \{\boldsymbol{q}_i^2\})|^2}{\prod_{i=1}^{2}[(m_p^2\xi_i^2 + \boldsymbol{q}_i^2)|\Phi_B(\xi_i, \boldsymbol{q}_i^2)|^2]}, \qquad (21)$$

where functions ρ_{ij}, $\bar{\Phi}_{ij}$ and Φ_B are given in Appendix A.

We are now ready to make predictions for high energies. Numerically calculated cross sections for the exclusive $D\pi E$ are shown in Fig. 8 and listed in Table 2 for parametrizations from Appendices B and C.

4 Extraction of $\pi^+ p$ and $\pi^+\pi^+$ cross sections. The role of absorption. Backgrounds

To extract $\pi^+ p$ and $\pi^+\pi^+$ cross sections from the $S\pi E$ and $D\pi E$ processes we can use (9) and (19). Let us rewrite these two equations in the following form:

$$\frac{d\sigma_{X,\pi^+p}(\xi s)}{d\Phi_X} = \frac{d\sigma_{X,S\pi E}}{d\xi\, dt\, d\Phi_X}\frac{E(s/s_0, \xi, t)}{S(s/s_0, \xi, t)}, \qquad (22)$$

$$\frac{d\sigma_{X,\pi^+\pi^+}(\xi_1\xi_2 s)}{d\Phi_X} = \frac{d\sigma_{X,D\pi E}}{d\xi_1\, d\xi_2\, dt_1\, dt_2\, d\Phi_X}$$

$$\times \frac{E(s/s_0, \xi_1, t_1)E(s/s_0, \xi_2, t_2)}{S_2(s/s_0, \{\xi_i\}, \{t_i\})}, \qquad (23)$$

where

$$E(s/s_0, \xi, t) = \frac{(t - m_\pi^2)^2}{-t}\frac{16\pi^2}{G_{\pi^+pn}^2 F^2(t)\xi^{1-2\alpha_\pi(t)}}. \qquad (24)$$

An exact extraction procedure is quite delicate. If we want to extract $\pi^+ p$ and $\pi^+\pi^+$ cross sections in a model-independent way, we have to take (22), (23) in the limit $t_i \to m_\pi^2$. For this limit we should extrapolate the parametrizations of the data on $S\pi E$ and $D\pi E$ differential cross sections to the positive $t_i = m_\pi^2$, i.e. beyond the physical region. Functions S and S_2 are equal to unity for this value of t_i, that is why the phenomenological model for these functions is not important. This procedure is actually the Chew–Low extrapolation method [22, 23].

Experimentally extrapolation to m_π^2 is rather difficult (see Sect. 5), since the errors in t are larger than m_π^2. To get around this problem we extract cross sections for pions with low virtualities and assume that the values (22), (23) are close to reality. It is clear from the fact that the main contribution to the cross section comes from the region $|t_i| < 0.25$ GeV^2 (see Fig. 6b). In this region the dependence of $\sigma_{\pi^+ p}$ ($\sigma_{\pi^+\pi^+}$) on t is assumed to be weak enough, i.e. pions are on-mass-shell.

Functions S and S_2 are close to unity in the physical region of negative t values (see Figs. 9, 10), and we can estimate errors of the model due to absorptive corrections. It was shown in [1] that such a model-dependent extraction works satisfactory for $\sqrt{s} < 70$ GeV. This fact is illustrated in Fig. 11a. All the parametrizations are close to the extracted values and the real data points, but for higher energies (Fig. 11b) the difference between models becomes larger.

To avoid singularities in the extrapolation procedure at $t = 0$ and model dependence in S and S_2 it is convenient to extrapolate quantities in the r.h.s. of (22) and (23) multiplied by St/m_π^2 and $S_2 t_1 t_2/m_\pi^4$ correspondingly. The behavior of St/m_π^2 is shown in Fig. 12. It is a smooth function of t in the whole region of the extrapolation. Practically we will have $\sigma_{\pi^+ p}St/m_\pi^2$ as a result of the extrapolation, which is equal to $\sigma_{\pi^+ p}$ at $t = m_\pi^2$.

The role of absorptive effects (i.e. model dependence of the final result) is significant if we want to extract πp and $\pi\pi$ cross sections from the $S\pi E$ and $D\pi E$ differential cross sections integrated in the wide region of t values, where absorption is strong. That is why we need an experimental instrument to measure differential cross sections for
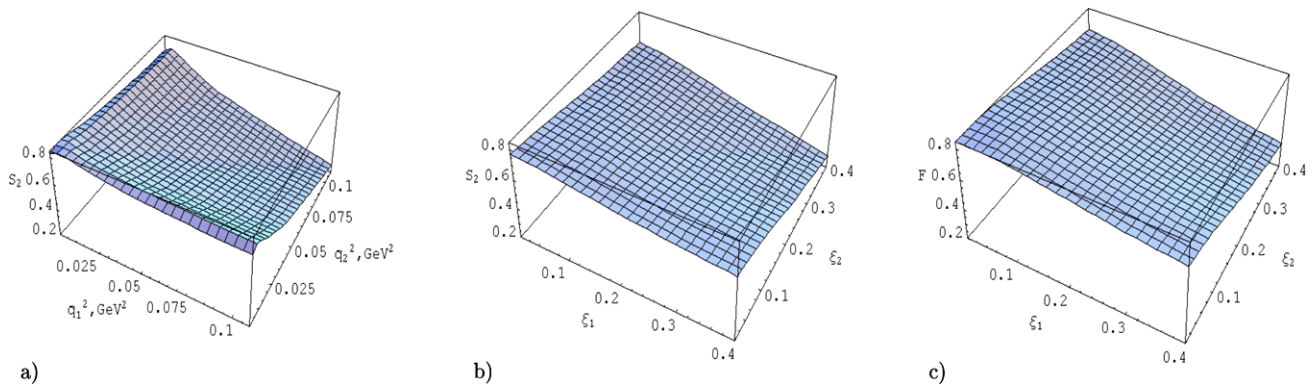
646

Eur. Phys. J. C (2010) 69: 641–655

Fig. 9 Function $S_2(s/s_0, \xi_{1,2}, |\boldsymbol{q}_{1,2}|)$ in the physical region of negative t values at $\sqrt{s} = 10$ TeV for: (**a**) for fixed $\xi_{1,2} = 0.01$ (**b**) for fixed $|\boldsymbol{q}_{1,2}| \sim 0$. (**c**) Function $F(\xi_1, \xi_2)$ at $\sqrt{s} = 10$ TeV
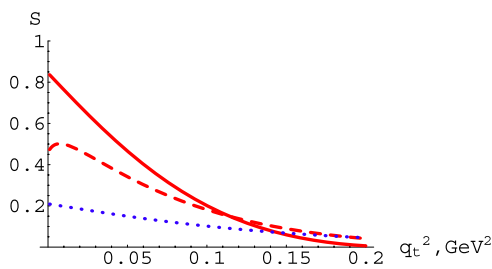

Fig. 10 Function $S(s/s_0, \xi, q_t)$ at $\sqrt{s} = 10$ TeV in the physical region of negative t values for three different fixed ξ values: $\xi = 0.3$ (*dotted*), $\xi = 0.1$ (*dashed*) and $\xi = 10^{-4}$ (*solid*). For low ξ and $|\boldsymbol{q}|$ function S is close to unity

low t values with good resolution. The present design of detectors does not allow t measurements, it gives only restriction $|t| < \sim 1.2$ GeV^2 [1]. If to assume a weak enough t-dependence of πp and $\pi\pi$ cross sections, then we could hope to extract these cross sections (though, with big errors) by the following procedure:

$$\sigma_{\pi^+ p}(\xi s) = \frac{\frac{d\sigma_{S\pi E}}{d\xi}}{\tilde{S}(\xi)}, \quad \tilde{S}(\xi) = \int_{t_{\min}}^{t_{\max}} dt \frac{S(s/s_0, \xi, t)}{E(s/s_0, \xi, t)},$$

$$\quad (25)$$

$$\tilde{S}_2(\xi_1, \xi_2) = \int_{t_{\min}}^{t_{\max}} dt_1 \, dt_2 \frac{S_2(s/s_0, \{\xi_i\}, \{t_i\})}{E(s/s_0, \xi_1, t_1) E(s/s_0, \xi_2, t_2)},$$

$$\sigma_{\pi^+\pi^+}(\xi_1 \xi_2 s) = \frac{\frac{d\sigma_{D\pi E}}{d\xi_1 d\xi_2}}{\tilde{S}_2(\xi_1, \xi_2)}. \quad (26)$$

Functions $\tilde{S}_2(\xi_1, \xi_2)$ and $\tilde{S}(\xi)$ are depicted in Fig. 13. To suppress theoretical errors of $\tilde{S}$ and $\tilde{S}_2$ we have to measure total and elastic pp rates at 10 TeV, since all the models for absorptive corrections are normalized to pp cross sections. At present we can estimate the theoretical error to be less than 10% for this method from predicted values of total pp cross sections in the most popular models (see Fig. 1a).

The case of the DπE is more complicated since the function S_2 is not factorizable. For low t_i it is approximately equal to

$$F(\xi_1, \xi_2) \equiv S_2(s/s_0, \xi_1, \xi_2, 0, 0)$$
$$\simeq \left(\sqrt{S(s/s_0, \xi_1, 0)} + \sqrt{S(s/s_0, \xi_2, 0)} \right.$$
$$\left. - \sqrt{S(s/s_0, \xi_1, 0) S(s/s_0, \xi_1, 0)} \right)^2, \quad (27)$$

which is clear from Figs. 9b, c.

To estimate total absorptive effect we have to take the ratio

$$S_{\text{tot}} = \int_{\Omega'} \frac{d\sigma}{d\Phi} \Big/ \int_{\Omega'} \frac{d\sigma_0}{d\Phi}, \quad (28)$$

$$\Omega' : \xi_{\min} = 10^{-3} < \xi_i < \xi_{\max},$$

$$0.01 \text{ GeV}^2 < |t| < 0.5 \text{ GeV}^2. \quad (29)$$

Φ is the phase space for the SπE (DπE), and $d\sigma_0/d\Phi$ is the cross section without absorptive corrections (i.e. for $S \equiv S_2 \equiv 1$). The results are listed in Table 3.

If we could measure momenta of all the final particles, we would have only exclusive backgrounds for our SπE and DπE signal processes with elastic $\pi^+ p$ (Fig. 4a) and $\pi^+\pi^+$ (Fig. 4c) scattering. The single low mass dissociative background for the exclusive SπE is depicted in Fig. 4b. For the exclusive DπE we have two exclusive backgrounds of Figs. 4d, e. In a real experiment we can detect only one or two particles in the final state, and we have to take into account all the inclusive backgrounds: single and double dissociation, central diffraction, minimum bias with neutrons production, inclusive single and double charge exchanges with π^+ (see Fig. 14) and also ρ, a_2 exchanges (for more exact estimations of inclusive backgrounds see Sect. 5).

Fig. 11 Total $\pi^+ p$ cross sections versus different parametrizations: [2] (*solid*), [3] (*dashed*), [4] (*dotted*) and [5, 6] (*dash-dotted*). (**a**) Real data from PDG (*triangles*) up to $\sqrt{s} = 25$ GeV and extracted values (*boxes*) up to $\sqrt{s} = 70$ GeV (see [1]); (**b**) total $\pi^+ p$ cross sections in the energy range 0.5 TeV $< \sqrt{s} < 7$ TeV
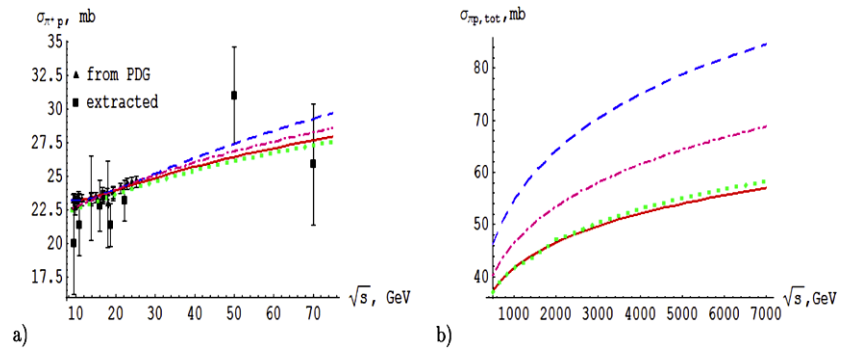
Fig. 12 Function $S(\xi, t) t/m_\pi^2$ versus t/m_π^2 at fixed $\xi = 0.05$. The boundary of the physical region $t_0 = -m^2 \xi^2/(1 - \xi)$ is represented by vertical *dashed line* in (**b**)
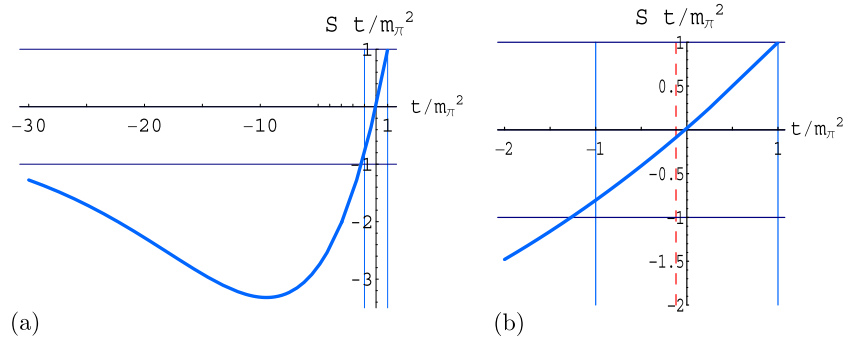
Fig. 13 Values of absorptive corrections integrated with form-factors in the region 0.01 GeV$^2 < |t_i| < 1.2$ GeV^2. (**a**) $\tilde{S}(\xi)$; (**b**) $\tilde{S}_2(\xi_1, \xi_2)$: $\xi_2 = \xi_1$ (*solid*), $\xi_2 = 0.1$ (*dashed*), $\xi_2 = 0.2$ (*dotted*) and $\xi_2 = 0.3$ (*dash-dotted*)
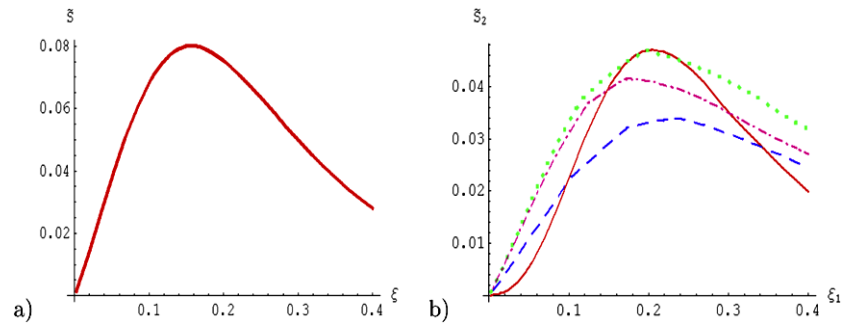
Table 3 Total absorptive corrections for exclusive $S\pi E$ and $D\pi E$ in the kinematical region 0.01 GeV$^2 < |t_i| < 0.5$ GeV^2, $\xi_{min} = 10^{-3} < \xi_i < \xi_{max}$ for parametrizations from Appendices B, C

ξ_{max}	0.05	0.1	0.2	0.3	0.4
$S_{tot, S\pi E}$	0.39	0.34	0.27	0.22	0.18
$S_{tot, D\pi E}$	0.47	0.41	0.33	0.26	0.25

5 Experimental possibilities

In this chapter we analyze CMS [24] capabilities to measure elastic $\pi^+ p$ and $\pi^+\pi^+$ scattering at 10 TeV, c.m. energy of LHC protons in the first runs. The CMS Zero Degree Calorimeters, ZDCs [25, 26], can measure leading neutrons in the exclusive $S\pi E$, $pp \rightarrow np\pi^+$ (Fig. 4a), and $D\pi E$, $pp \rightarrow n\pi^+\pi^+ n$ (Fig. 4c), processes.[1] The ZDCs are located

Fig. 14 Inclusive $S\pi E$ (**a, b, c**) and $D\pi E$ (**d, e, f**) backgrounds. (**a**) single dissociation, (**b**) double dissociation, (**c**) minimum bias in the $\pi^+ p$ channel, and (**d**) single dissociation, (**e**) double dissociation, (**f**) minimum bias in the $\pi^+\pi^+$ channel

---

[1] Further, exclusive $S\pi E$ ($D\pi E$) elastic events, i.e. $S\pi E$ ($D\pi E$) with $\pi^+_{virt} p$ ($\pi^+_{virt}\pi^+_{virt}$) scattering elastically, will be designated as $S\pi E_{elastic}$ ($D\pi E_{elastic}$) for brevity.
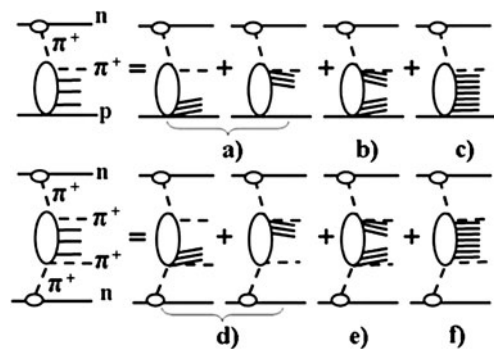
between the two beam pipes at ≈ 140 m on each side of the interaction point. They are able to measure the energy of forward neutral particles in the pseudorapidity region $|\eta| > 8.5$.

SπE and DπE events have been generated in the framework of the simulation package EDDE [27]. The kinematics of the SπE and DπE processes are defined by ξ_n and t_n of the leading neutron. The $p\pi_{virt}^+ n$ vertex is generated on the basis of the model described in [1]. For the simulation of $\pi_{virt}^+ p$ and $\pi_{virt}^+ \pi_{virt}^+$ elastic scattering PYTHIA 6.420 [28] has been used. Obviously, π_{virt}^+ and p (π_{virt}^+ and π_{virt}^+) can interact inelastically and diffractively. Then, in the diffractive interaction of π_{virt}^+ and p, either the π_{virt}^+ or the p, or both of them, can dissociate. All of these processes have been studied as backgrounds, as well as minimum bias and diffractive pp events. Diagrams for some of the background processes are shown in Fig. 14. Signal and background have been generated by EDDE v.3.0.0 and PYTHIA 6.420. The SπE cross section, including all types of $\pi_{virt}^+ p$ interactions, is estimated to be about 2.6 mb at 10 TeV and $\xi_n < 0.4$ [1]. Corresponding cross sections for the signal and backgrounds are listed below.

Signal:

– SπE$_{elastic}$: $\sigma_{pp \to np\pi^+} = 0.33$ mb.

Backgrounds from pp and inelastic SπE events:

– minimum bias events: $\sigma_{pp \to X} = 50$ mb;
– single diffractive dissociation: $\sigma_{pp \to pX} = 14$ mb;
– double diffractive dissociation: $\sigma_{pp \to XY} = 9.7$ mb;
– SπE, minimum bias in the $\pi_{virt}^+ p$ channel, Fig. 14c: $\sigma_{pp \to nX} = 1.54$ mb;
– SπE, single diffraction in the $\pi_{virt}^+ p$ channel with proton dissociation, Fig. 14a: $\sigma_{pp \to n\pi^+ X} = 0.23$ mb;
– SπE, single diffraction in the $\pi_{virt}^+ p$ channel with $\pi+$ dissociation, Fig. 14a: $\sigma_{pp \to npX} = 0.20$ mb;
– SπE, double diffraction in the $\pi_{virt}^+ p$ channel, Fig. 14b: $\sigma_{pp \to nXY} = 0.27$ mb.

Figure 15 shows the ratio of events for SπE$_{elastic}$ (shadowed) and background processes. On the picture minimum bias processes have numbers less than 90 and diffractive processes have numbers 92, 93 and 94, according to PYTHIA's definition. All SπE processes are placed between numbers 400 and 500 and DπE processes are in the region from 500 to 600 in our generation. Signal processes, SπE$_{elastic}$ and DπE$_{elastic}$, have numbers 491 and 591 respectively. SπE$_{elastic}$ events contribute ~ 0.4% to the total cross sections, DπE$_{elastic}$ events is around 0.025% only. DπE events have been simulated by the same method, as SπE, using EDDE v.3.0.0 and PYTHIA 6.420. DπE cross section, including all types of $\pi_{virt}^+ \pi_{virt}^+$ interactions, is estimated to be about 200 μb at 10 TeV and $\xi_{n1,n2} < 0.4$ [1]. Corresponding cross sections for the signal and inelastic DπE backgrounds are listed below.

Signal:

– DπE$_{elastic}$: $\sigma_{pp \to n\pi^+\pi^+ n} = 24$ μb.

Backgrounds from inelastic DπE events:

– DπE, minimum bias in the $\pi_{virt}^+ \pi_{virt}^+$ channel, Fig. 14f: $\sigma_{pp \to nXn} = 124$ μb;
– DπE, single diffraction in the $\pi_{virt}^+ \pi_{virt}^+$ channel, Fig. 14d: $\sigma_{pp \to n\pi^+ Xn} = 30$ μb;
– DπE, double diffraction in the $\pi_{virt}^+ \pi_{virt}^+$ channel, Fig. 14e: $\sigma_{pp \to nXYn} = 22$ μb.

Inelastic and diffractive pp interactions produce background events for DπE$_{elastic}$, as well as for SπE$_{elastic}$. Moreover, SπE elastic and inelastic processes produce strong backgrounds for DπE$_{elastic}$, in addition to the inelastic pp and DπE. And, on the contrary, DπE elastic and inelastic events can imitate SπE$_{elastic}$.

In our simulation, cross sections for the SπE$_{elastic}$ and DπE$_{elastic}$ signals, depend on $\pi_{virt}^+ p$ and $\pi_{virt}^+ \pi_{virt}^+$ elastic scattering models integrated to the PYTHIA 6.420. It is interesting to note that values obtained for these cross sections are very close to the ones which can be calculated in the BSW [4] and GP [5, 6] parametrizations, see Tables 1 and 2. The ratio between the SπE elastic (signal) and inelastic (part of background) events are presented in Fig. 16a. Figure 16b shows the same for DπE.

As in paper [1], for SπE selections we choose events with neutrons in the forward or backward ZDC and with the absence of neutrons in the opposite one:

$$\begin{bmatrix} N_n^f > 0 & \& & N_n^b = 0, \\ N_n^b > 0 & \& & N_n^f = 0. \end{bmatrix} \tag{30}$$

For the DπE, we selected events with neutrons in both the forward and backward ZDCs:

$$N_n^f > 0 \quad \& \quad N_n^b > 0. \tag{31}$$

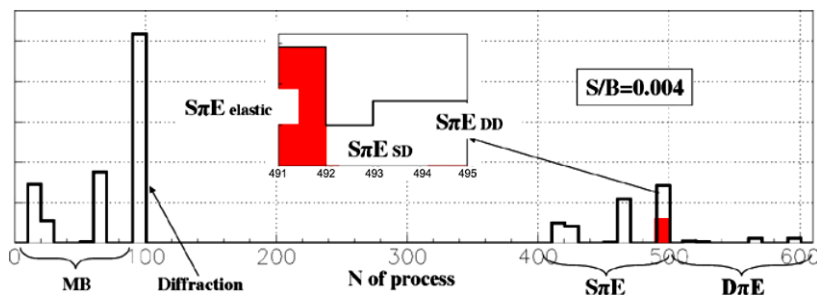**Fig. 15** Events ratio for SπE$_{elastic}$ (*shadowed*) and background

Fig. 16 (**a**) $S\pi E$ elastic (*solid*) and total (*dotted*) events distribution versus the $(\pi^{+}_{\mathrm{virt}} p)$ invariant mass; (**b**) $D\pi E$ elastic (*solid*) and total (*dotted*) events distribution versus the $(\pi^{+}_{\mathrm{virt}}\pi^{+}_{\mathrm{virt}})$ invariant mass
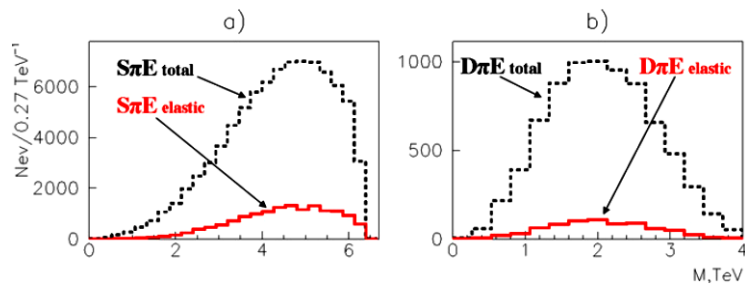

Fig. 17 The ratio of events for the signal $S\pi E_{\mathrm{elastic}}$ (*shadowed*) and background processes after the selection (30)
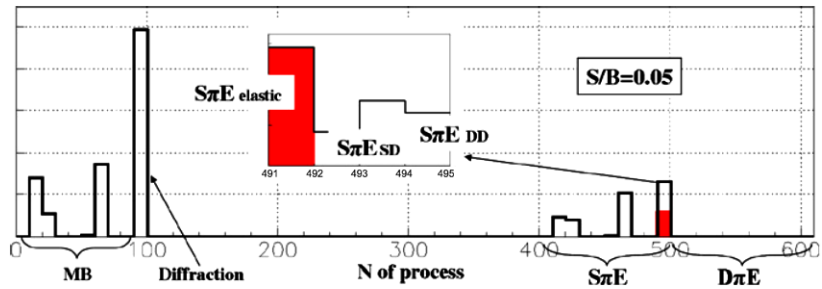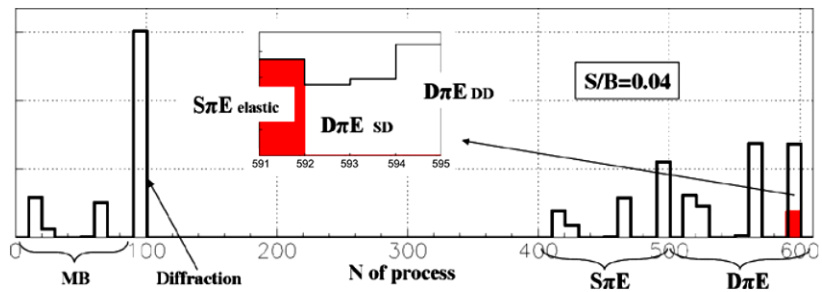

Fig. 18 The ratio of events for the signal $D\pi E_{\mathrm{elastic}}$ (*shadowed*) and background processes after the selection (31)

Here, N_n^f (N_n^b) is the number of neutrons hitting the forward (backward) ZDC. Such selections suppress the background for $S\pi E_{\mathrm{elastic}}$ ($D\pi E_{\mathrm{elastic}}$) events by a factor 14 (160). The signal to background ratio becomes equal to 0.05 for the $S\pi E_{\mathrm{elastic}}$ and 0.04 for the $D\pi E_{\mathrm{elastic}}$. Figure 17 shows the ratio of events for $S\pi E_{\mathrm{elastic}}$ (shadowed) and background processes after the selection (30). The same picture is plotted for the $D\pi E_{\mathrm{elastic}}$ signal and background after the selection (31), Fig. 18.

The signal $S\pi E_{\mathrm{elastic}}$ ($pp \to n\pi^{+}p$) event has neutron, proton and π^{+} in the final state. Apart from neutrons, which can be detected by ZDC, two other particles move out of the CMS acceptance. The proton, scattered elastically, should move inside the beam pipe. The π^{+} meson should fly in the same direction as the neutron and it is scattered on a small angle too (see Fig. 19b). In the LHC beam pipe π^{+} mesons are deflected by magnets and hit the pipe producing hadron showers. This could be used for π^{+} mesons detection by scintillating counters that is discussed below. Thus, though it looks as a paradox, we should demand absence of a signal in the CMS detectors, except for the one of ZDCs, for the $S\pi E_{\mathrm{elastic}}$ trigger. For example, we could select events with

zero signal in the CMS calorimeters:

$$\begin{cases} N_{\mathrm{BARREL}} = 0, \\ N_{\mathrm{ENDCAP}} = 0, \\ N_{\mathrm{HF}} = 0, \\ N_{\mathrm{CASTOR}} = 0. \end{cases} \qquad (32)$$

Figure 20 shows the efficiency of such selection for the $S\pi E_{\mathrm{elastic}}$. The signal to background ratio becomes equal to 1, i.e. we have achieved improvement 18 times better in comparison with the previous selection (30). Detailed study of the rest of backgrounds (left bin on the Fig. 20) has shown that it contains processes of the single diffractive dissociation, $pp \to pN^{*} \to pn\pi^{+}$, where the pomeron exchange leads to the proton excitation N^{*} and its subsequent decay to the π^{+} meson and neutron (see the diagram on the Fig. 20). This reaction can imitate the $S\pi E_{\mathrm{elastic}}$ process as well. However, the further careful study of both reactions has shown some difference in their kinematics. Thus, t distributions of neutrons have different slope parameters. It could improve the signal/background ratio up to the value 1.7 by the selection $|t_n| < 0.2$ GeV^2, Fig. 19a.
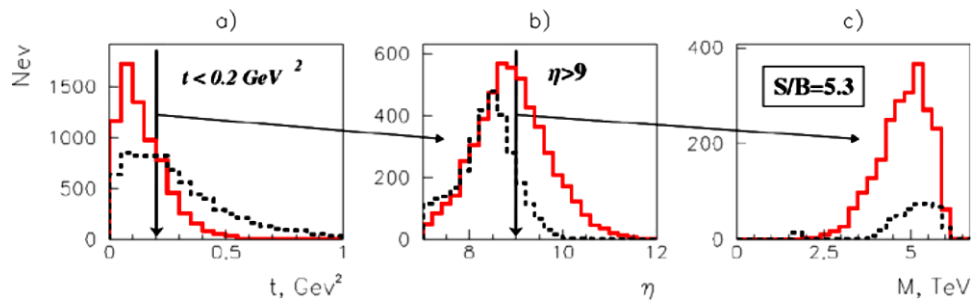
650

Eur. Phys. J. C (2010) 69: 641–655

Fig. 19 (a) t of the leading neutron for the signal $S\pi E_{elastic}$ (*solid*) and background (*dotted*) after selections (30) & (32); (b) η of the π^+ for the signal $S\pi E_{elastic}$ (*solid*) and background (*dotted*) after selections (30) & (32) & $t_n < 0.2$ GeV^2; (c) the $(\pi^+ p)$ mass distribution for the signal $S\pi E_{elastic}$ (*solid*) and background (*dotted*) after selections (30) & (32) & $t_n < 0.2$ GeV^2 & $\eta_{\pi^+} > 8.5$

Fig. 20 The ratio of events for the signal $S\pi E_{elastic}$ (*shadowed*) and background processes after selections (30) & (32)
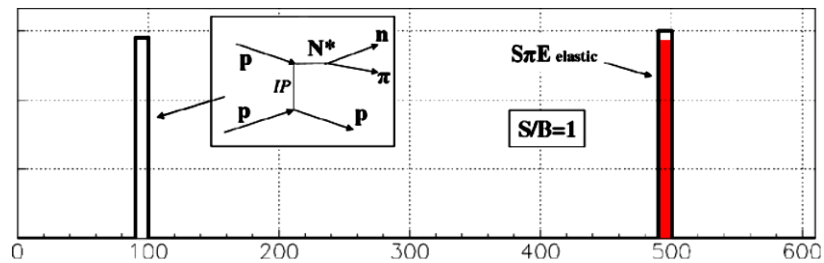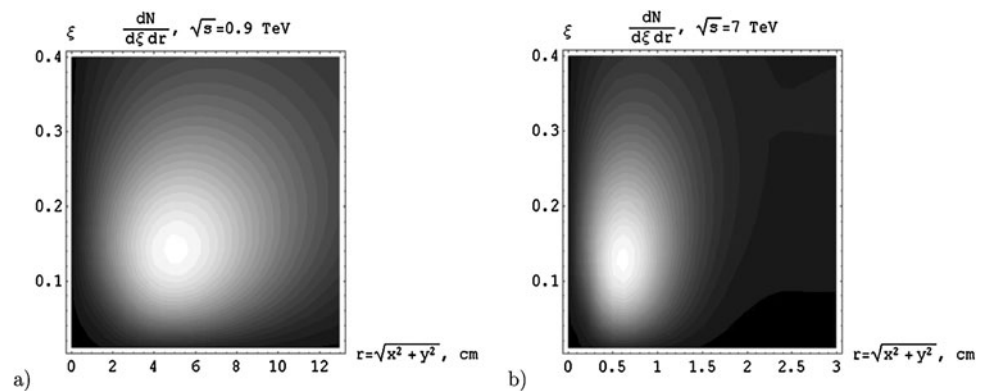

Fig. 21 $dN/d\xi\,dr$ for (**a**) $\sqrt{s} = 900$ GeV and (**b**) 7 TeV

Each of the CMS ZDCs consist of two sections, an electromagnetic, EM, part for measuring photons, π_0, ηs etc. and a hadronic part designed to measure neutral hadrons such as neutrons and λs [26]. The energy resolution of the detector for hadrons is $138\%/\sqrt{E} + 13\%$. The electromagnetic part is divided into strips that run in the vertical direction. These strips can be used to measure the horizontal position of the particle's impact point with a resolution of about 0.4 cm. The hadronic part that has is divided into 4 depth segments but has no transverse segmentation. About 1/3rd of the time neutrons will start to shower in the electromagnetic part and for these neutrons we can extract some position information. The ZDCs can also be used to select events in the CMS level one trigger.

The geometrical acceptance of the calorimeter is ± 4.4 cm horizontally and ± 5.0 vertically. For CMS the LHC beams cross in the horizontal plane and so the nominal position

of the zero degree point will vary depending on the crossing angle. For example if the crossing angle of the beam is 140 µradians the zero degree point will be at $x = +2$ cm. Given the energy and position resolution of the detector it may be possible to make a rough measurement of the angular distribution of the neutrons.

The only independent measurements that the ZDCs can make of the neutrons are the energy loss ξ and the distance from the collision axis $r = \sqrt{x^2 + y^2}$. Figures 21, 22 and 23 show the distribution of neutrons, their t value and the resolution of t versus ξ and r for (a) $\sqrt{s} = 900$ GeV and (b) 7 TeV. As the energy increases the radial distribution tends to shrink toward $r = 0$. Given the current limited position resolution of the ZDC it may be possible to gain some information about the t distribution at $\sqrt{s} = 900$ GeV. However for multi TeV energies it will probably be necessary to upgrade the detector.

Fig. 22 The t value for neutrons as a function of distance from the collision axis and ξ for (**a**) $\sqrt{s} = 900$ GeV and (**b**) 7 TeV
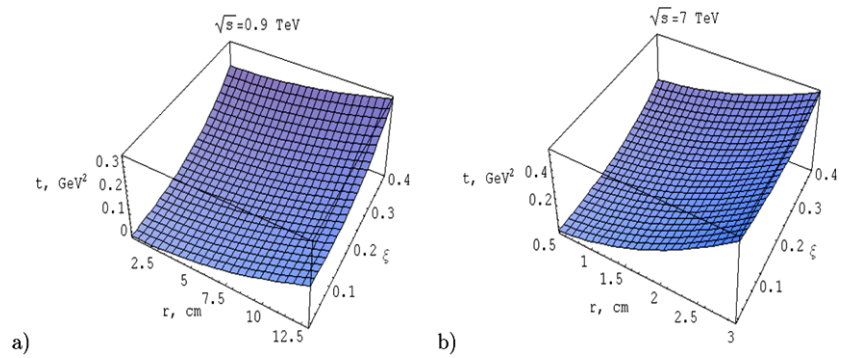

Fig. 23 The relative resolution for t, i.e. $\delta t/t$ value for neutrons as a function of distance from the collision axis and ξ for (**a**) $\sqrt{s} = 900$ GeV and (**b**) 7 TeV. We have assumed that $\delta r = 0.5$ cm, distance from the detector to the interaction point is 140 m and $\delta\xi/\xi \simeq 0.14$
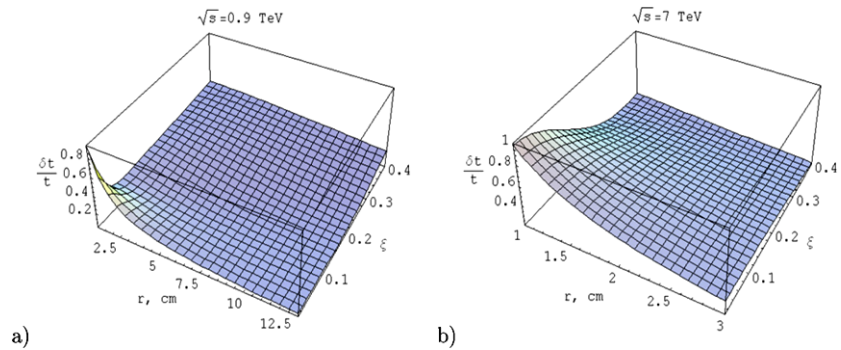

Fig. 24 The ratio of events for the signal $D\pi E_{elastic}$ (*shadowed*) and background processes after selections (31) & (32)
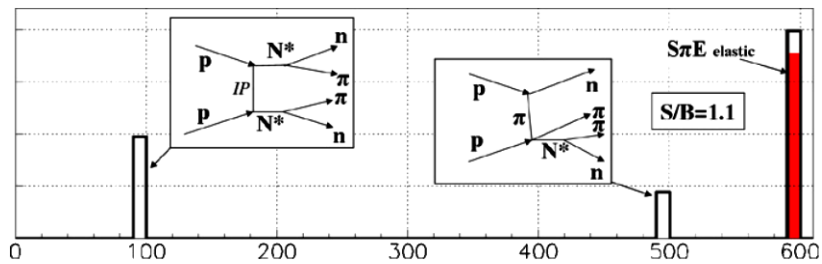

Figure 19(b) shows that the π^+ mesons are deflected a bit stronger for the signal than for a background, If we could have counters for charge particles in the pseudorapidity region $\eta > 9$, it would allow us to improve the signal/background ratio up to 5 and higher, Fig. 19c. The possibility of such counters' installation along the LHC beam on both sides of the CMS was studied in [29]. Set of FSCs, placed at distances from 60 to 140 m from the interaction point, could cover the pseudorapidity region from 8 to 11. They could register particle showers induced by the primary π^+ with high efficiency, up to 70%. Unfortunately, in the present setup of the forward CMS detectors there are no forward counters and present design of the ZDC does not allow one to measure t of the leading neutron. So, this is a task for the future.

Selections (32), applied to the $D\pi E_{elastic}$, improve the signal/background ratio up to 1.1 (see Fig. 24). The rest of the background comes from the double diffractive dissociation $pp \to N^*N^* \to n\pi^+\pi^+n$ (the left diagram on Fig. 24) and from the $S\pi E$ events produced by single diffraction in

the $\pi^+ p$ channel with the subsequent decay of the excited protons to π^+ and neutron (the right diagram on Fig. 24). t distributions for signal and background are different, as it is shown on Fig. 25a. As for the $S\pi E$, we could improve the signal/background ratio up to ~ 2 by selections:

$$\begin{cases} |t_n^f| < 0.25 \text{ GeV}^2, \\ |t_n^b| < 0.25 \text{ GeV}^2, \end{cases} \quad (33)$$

using (33) in a combination with (31) and (32). For further improvements of data we could use different deviation of π meson from the beam axis for signal and background, Fig. 25b. Selections

$$\begin{cases} \eta_n^f > 9, \\ \eta_n^b > 9, \end{cases} \quad (34)$$

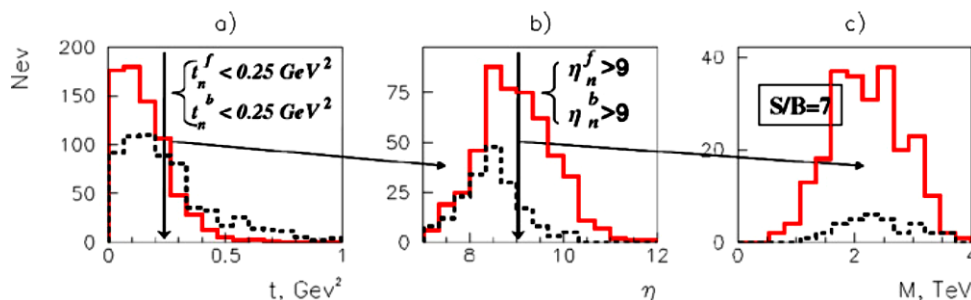give a data sample with a signal/background ratio ~ 7, see Fig. 25c.

Fig. 25 (**a**) t of the leading neutrons for the signal $D\pi E_{\text{elastic}}$ (*solid*) and background (*dotted*) after selections (31) & (32); (**b**) η of the π^+ mesons for the signal $D\pi E_{\text{elastic}}$ (*solid*) and background (*dotted*) after selections (31) & (32) & (33); (**c**) the $(\pi^+\pi^+)$ mass distribution for the signal $D\pi E_{\text{elastic}}$ (*solid*) and background (*dotted*) after selections (31) & (32) & (33) & (34)

6 Discussions and conclusions

In conclusion, our study of $S\pi E_{\text{elastic}}$ and $D\pi E_{\text{elastic}}$ processes shows that with present setup of the forward detectors we could expect observation of $S\pi E_{\text{elastic}}$ and $D\pi E_{\text{elastic}}$ events mixing with background in the proportion $\sim$1:1. Rough estimations on the generator level shows that we could observe $\sim 10^8$ $S\pi E_{\text{elastic}}$ events distributed in the mass region from 1 to 6 TeV and $\sim 10^7$ $D\pi E_{\text{elastic}}$ events distributed in the mass region from 0.5 to 4 TeV at the integrated luminosity 1 pb^{-1}. As it was said they will be mixed with approximately the same amount of background events. Improvement of the data purity demands a considerable modernization of the forward detectors. Some modification of the ZDC is required to measure the t of the leading neutrons. It would be very useful to install forward shower counters FSCs along the beam at distances from 60 to 140 m for the detection of elastic scattered π-mesons in the region $\eta > 8$ would improve the measurements significantly. Realization of such modifications is beyond this article.

Theoretically, it is very interesting to have both elastic and total cross sections of πp and $\pi\pi$ scattering. At present we could only use the extraction procedure for t-integrated $S\pi E$ and $D\pi E$ cross sections (25), (26) which is far from the ideal one (22), (23). Rough estimations give the model error about 10%. The main part of this error comes from the uncertainties in the absorptive corrections which are normalized to pp total and elastic cross sections. Measurements of the pp total cross section, which would be done by the TOTEM experiment at LHC, can improve the precision of our model-dependent extraction procedure significantly. We would like to stress again, that model-independent extraction procedure for πp and $\pi\pi$ total and elastic cross sections makes precision measurements of t of the leading neutron at small angles mandatory.

In spite of all the difficulties, proposed tasks are of exceptional importance, and we hope that they will push modernization of the forward detectors for future precise measurements.

Appendix A

Here we define functions for the calculation of absorptive corrections for the $S\pi E$ and the $D\pi E$ processes. For the $S\pi E$ we have:

$$\Phi_B\left(\xi, \boldsymbol{q}^2\right)$$
$$= \frac{N(\xi)}{2\pi}\left(\frac{1}{\boldsymbol{q}^2 + \epsilon^2} + \iota\frac{\pi\alpha'_\pi}{2(1-\xi)}\right)\exp\left(-\beta^2\boldsymbol{q}^2\right)$$
$$\simeq \frac{N(\xi)}{2\pi}\frac{1}{\boldsymbol{q}^2 + \epsilon^2}\frac{1}{1 + \beta^2\boldsymbol{q}^2}, \quad \boldsymbol{q} \to 0, \tag{A.1}$$

$$N(\xi) = (1-\xi)\frac{G_{\pi^+pn}}{2}\xi^{\frac{\alpha'_\pi\epsilon^2}{1-\xi}}\exp\left[-b\frac{m_p^2\xi^2}{1-\xi}\right], \tag{A.2}$$

$$\beta^2 = \frac{b + \alpha'_\pi\ln\frac{1}{\xi}}{1-\xi}, \qquad \epsilon^2 = m_p^2\xi^2 + m_\pi^2(1-\xi), \tag{A.3}$$

$$\Phi_0 = \frac{N(\xi)}{2\pi}\int_0^\infty db\,\Theta_0\left(b, \xi, |\boldsymbol{q}|\right)V(b), \tag{A.4}$$

$$|\boldsymbol{q}|\Phi_s = \frac{N(\xi)}{2\pi}\int_0^\infty db\,\Theta_s\left(b, \xi, |\boldsymbol{q}|\right)V(b), \tag{A.5}$$

$$\Theta_0\left(b, \xi, |\boldsymbol{q}|\right) = \frac{bJ_0(b|\boldsymbol{q}|)(K_0(\epsilon b) - K_0(\frac{b}{\beta}))}{1 - \beta^2\epsilon^2}, \tag{A.6}$$

Table 4 Parameters of the model [8]

i	c_i	r_i^2 (GeV^{-2})
1	53.0 ± 0.8	6.3096 ± 0.2522
2	9.68 ± 0.16	3.1097 ± 0.1817
3	1.67 ± 0.07	2.4771 ± 0.0964

Table 5 Parameters of the model [4]

c	c'	m_1	m_2	$m_{3\pi}$
0.167	0.748	0.577225	1.719896	0.7665

f_π	a_π	f	a
4.2414	2.3272	6.970913	1.858442

$$\Theta_s(b, \xi, |\boldsymbol{q}|)$$

$$= \frac{b J_1(b|\boldsymbol{q}|)(\epsilon K_1(\epsilon b) - \frac{1}{\beta} K_1(\frac{b}{\beta}))}{1 - \beta^2 \epsilon^2}, \tag{A.7}$$

$$V(b) = \exp\left(-\Omega_{\text{el}}(s/s_0, b)\right), \tag{A.8}$$

$$\Omega_{\text{el}} = \sum_{i=1}^{3} \Omega_i, \tag{A.9}$$

$$\Omega_i = \frac{2c_i}{16\pi B_i} \left(\frac{s}{s_0} e^{-i\frac{\pi}{2}}\right)^{\alpha_{\text{IP}_i}(0)-1} \exp\left[-\frac{b^2}{4B_i}\right], \tag{A.9}$$

$$B_i = \alpha'_{\text{IP}_i} \ln\left(\frac{s}{s_0} e^{-i\frac{\pi}{2}}\right) + \frac{r_i^2}{4}, \tag{A.10}$$

the values of parameters can be found in (12) and in Table 4.

For the DπE process we can write the following expressions:

$$\bar{\Phi}_{ij} = \frac{N(\xi_1)N(\xi_2)}{(2\pi)^2} \int_0^\infty db_1 \, db_2 \, I_\phi(b_1, b_2)$$

$$\times \Theta_i(b_1, \xi_1, |\boldsymbol{q}_1|)\Theta_j(b_2, \xi_2, |\boldsymbol{q}_2|), \tag{A.11}$$

$$I_\phi(b_1, b_2) = \int_0^\pi \frac{d\phi}{\pi} V\left(\sqrt{b_1^2 + b_2^2 - 2b_1 b_2 \cos\phi}\right), \tag{A.12}$$

$$\rho_{00} = m_p^2 \xi_1 \xi_2, \qquad \rho_{0s} = m_p \xi_1,$$

$$\rho_{s0} = m_p \xi_2, \qquad \rho_{ss} = 1. \tag{A.13}$$

Appendix B

For the calculation of elastic cross sections we use the Bourrely–Soffer–Wu (BSW) parametrization [4]. Functions and values of parameters are given below.

$$T(s, t_p) = i \int_0^\infty b \, db \, J_0(b\sqrt{-t_p})\left(1 - e^{-\Omega_0(s,b)}\right), \tag{B.1}$$

$$\frac{d\sigma_{\text{el}}}{dt_p} = \pi \left|T(s, t_p)\right|^2, \tag{B.2}$$

$$\Omega_0(s, b) = \Omega_{\text{IP}} + \sum_i \Omega_i, \tag{B.3}$$

$$\Omega_{\text{IP}} \simeq \frac{s^c}{\ln^{c'} s}\left[1 + \frac{e^{i\pi c}}{(1 + \frac{i\pi}{\ln s})^{c'}}\right] F_{\text{BSW}}(b)$$

$$\text{for } s \gg m_p^2, |t|. \tag{B.4}$$

Table 6 Parameters of the model [4] for secondary reggeons in pp scattering

i	ω	A_2	ρ
b_i, GeV^{-2}	0	0	8.54
C_i	-167.3293	-24.2686	124.91969
$\alpha_i(t)$	$0.3229 + 0.7954t$	$0.3566 + t$	$0.3202 + t$

For the $\pi^+ p$ elastic scattering we have $i = \rho$ in (B.3) and

$$F_{\text{BSW}}^{\pi^+ p}(b) = \int_0^\infty q \, dq \, J_0(qb) f_\pi \frac{a_\pi^2 - q^2}{a_\pi^2 + q^2}$$

$$\times \frac{1}{(1 + \frac{q^2}{m_1^2})(1 + \frac{q^2}{m_2^2})(1 + \frac{q^2}{m_{3\pi}^2})}, \tag{B.5}$$

$$\Omega_\rho \simeq C_\rho(1 + i)\left(\frac{s}{s_0}\right)^{\alpha_\rho(0)-1} \frac{e^{-\frac{b^2}{4B_\rho}}}{2B_\rho}, \tag{B.6}$$

$$B_\rho = b_\rho + \alpha'_\rho(0) \ln\frac{s}{s_0}, \qquad b_\rho = 4.2704, \tag{B.7}$$

$$\alpha_\rho(t) = 0.3202 + t, \qquad C_\rho = 4.1624, \tag{B.8}$$

where values of parameters are listed in Table 5.

For the pp elastic scattering $i = \omega, A_2, \rho$ and

$$F_{\text{BSW}}^{pp}(b) = \int_0^\infty q \, dq \, J_0(qb) f \frac{a^2 - q^2}{a^2 + q^2}$$

$$\times \frac{1}{(1 + \frac{q^2}{m_1^2})^2(1 + \frac{q^2}{m_2^2})^2}, \tag{B.9}$$

$$\Omega_i(b) = \int_0^\infty q \, dq \, J_0(qb) C_i e^{-b_i q^2}$$

$$\times \left(1 \pm e^{-i\pi\alpha_i(-q^2)}\right)\left(\frac{s}{s_0}\right)^{\alpha_i(-q^2)}. \tag{B.10}$$

Values of parameters are listed in Table 6.

In this paper we take the following parametrization of the $\pi^+\pi^+$ elastic scattering, which is based on the BSW [4] one

654

Eur. Phys. J. C (2010) 69: 641–655

(approximate expressions for $s \gg s_0$, $|t| \ll 1$ GeV^2)

$$F_{\text{BSW}}^{\pi^+ \pi^+}(b)$$
$$\simeq \int_0^\infty q \, dq \, J_0(qb) f_{\pi\pi} \frac{a_{\pi\pi}^2 - q^2}{a_{\pi\pi}^2 + q^2} \frac{1}{(1 + \frac{q^2}{m_{3\pi}^2})^2}, \quad \text{(B.11)}$$

$$\Omega_0 \simeq \Omega_{\text{IP}}, \qquad f_{\pi\pi} = \frac{f_\pi^2}{f}, \qquad \frac{1}{a_{\pi\pi}^2} = \frac{2}{a_\pi^2} - \frac{1}{a^2}. \quad \text{(B.12)}$$

Appendix C

Another parametrization for pp, $\pi^+ p$ and $\pi^+ \pi^+$ cross sections is taken from [5, 6]. The scattering amplitude is represented in the usual eikonal form

$$T(s, b) = \frac{e^{2i\delta(s,b)} - 1}{2i} \quad \text{(C.1)}$$

(here $T(s, b)$ is the amplitude of the elastic scattering in the impact parameter b space, s is the invariant mass squared of colliding particles and $\delta(s, b)$ is the eikonal function). Amplitudes in the impact parameter space and momentum one are related thorough the Fourier–Bessel transforms

$$f(s, b) = \frac{1}{16\pi s} \int_0^\infty d(-t) J_0(b\sqrt{-t}) f(s, t), \quad \text{(C.2)}$$

$$f(s, t) = 4\pi s \int_0^\infty db^2 J_0(b\sqrt{-t}) f(s, b). \quad \text{(C.3)}$$

The eikonal function in the momentum space is

$$\delta(s, t) = \delta_{\text{P}}(s, t) + \delta_f(s, t)$$
$$= \left(i + \text{tg} \frac{\pi(\alpha_{\text{P}}(t) - 1)}{2} \right) \beta_{\text{P}}(t) \left(\frac{s}{s_0} \right)^{\alpha_{\text{P}}(t)}$$
$$+ \left(i + \text{tg} \frac{\pi(\alpha_f(t) - 1)}{2} \right) \beta_f(t) \left(\frac{s}{s_0} \right)^{\alpha_f(t)}. \quad \text{(C.4)}$$

The parametrization for the pomeron residue is

$$\beta_{\text{P}}(t) = B_{\text{P}} e^{b_{\text{P}} t} \left(1 + d_1 t + d_2 t^2 + d_3 t^3 + d_4 t^4 \right), \quad \text{(C.5)}$$

which is approximately (at low values of d_1, d_2, d_3 and d_4) an exponential at low t values. Residues of secondary reggeons we set as exponentials:

$$\beta_f(t) = B_f e^{b_f t}. \quad \text{(C.6)}$$

Phenomenological parametrization for the "soft" pomeron trajectory is set to

$$\alpha_{\text{P}}(t) = 1 + p_1 \left[1 - p_2 t \left(\text{arctg}(p_3 - p_2 t) - \frac{\pi}{2} \right) \right]. \quad \text{(C.7)}$$

Table 7 Values of parameters of the model [5, 6] for the pp scattering

Pomeron		f_2-reggeon	
p_1	0.123	c_f	0.1 GeV^2
p_2	1.58 GeV^{-2}	B_f	153
p_3	0.15	b_f	4.7 GeV^{-2}
B_{P}	43.5	$\alpha_f(0)$	0.78
b_{P}	2.4 GeV^{-2}	$\alpha'_f(0)$	0.63 GeV^{-2}
d_1	0.43 GeV^{-2}	ω-reggeon	
d_2	0.39 GeV^{-4}		
d_3	0.051 GeV^{-6}	c_ω	0.9 GeV^2
d_4	0.035 GeV^{-8}	B_ω	46
$\alpha_{\text{P}}(0)$	1.123	b_ω	5.6 GeV^{-2}
$\alpha'_{\text{P}}(0)$	0.28 GeV^{-2}	$\alpha_\omega(0)$	0.64
		$\alpha'_\omega(0)$	0.07 GeV^{-2}

Table 8 Values of parameters of the model [5, 6] for the elastic $\pi^\pm p$ scattering

B_{P}	26.7
b_{P}	2.36 GeV^{-2}
d_1	0.38 GeV^{-2}
d_2	0.30 GeV^{-4}
d_3	-0.078 GeV^{-6}
d_4	0.04 GeV^{-8}
B_f	67
b_f	1.88 GeV^{-2}

Trajectories of secondary reggeons f_2 and ω are parametrized by functions

$$\alpha_{\text{R}}(t) = \left(\frac{8}{3\pi} \alpha_s(\sqrt{-t} + c_{\text{R}}) \right)^{1/2}, \quad \text{R} = f, \omega, \quad \text{(C.8)}$$

where

$$\alpha_s(\mu) = \frac{4\pi}{11 - \frac{2}{3} n_f} \left(\frac{1}{\ln \frac{\mu^2}{\Lambda^2}} + \frac{1}{1 - \frac{\mu^2}{\Lambda^2}} \right) \quad \text{(C.9)}$$

is the one-loop analytic QCD running coupling [30], $n_f = 3$ is the number of flavors, $\Lambda \equiv \Lambda^{(3)} = 0.346$ GeV [31]. Parameters $c_f, c_\omega > 0$ are rather small to spoil the asymptotic behavior of secondary trajectories in the perturbative domain.

Residues for $\pi\pi$, πp and pp scattering are assumed to be

$$\beta_{\text{P}}^{\pi\pi}(t) = \frac{\beta_{\text{P}}^{\pi p}(t) \beta_{\text{P}}^{\pi p}(t)}{\beta_{\text{P}}^{pp}(t)}, \quad \text{(C.10)}$$

$$\beta_f^{\pi\pi}(t) = \frac{\beta_f^{\pi p}(t) \beta_f^{\pi p}(t)}{\beta_f^{pp}(t)}. \quad \text{(C.11)}$$

Parameters of the model are listed in Tables 7, 8.

Eur. Phys. J. C (2010) 69: 641–655

655

References

1. V. Petrov, R. Ryutin, A. Sobol, Eur. Phys. J. C **65**, 637 (2010)
2. A. Donnachie, P.V. Landshoff, Phys. Lett. B **296**, 227 (1992)
3. COMPETE Collaboration, B. Nicolescu et al., in *Pruhonice 2001, Elastic and Diffractive Scattering*, pp. 265–274. arXiv:hep-ph/0110170
4. C. Bourrely, J. Soffer, T.T. Wu, Eur. Phys. J. C **28**, 97 (2003)
5. A.A. Godizov, V.A. Petrov, J. High Energy Phys. **0707**, 083 (2007)
6. A.A. Godizov, Yad. Fiz. **71**, 1822 (2008)
7. M. Honda, M. Nagano, S. Tonwar, K. Kasahara, T. Hara, N. Hayashida, Y. Matsubara, M. Teshima, S. Yoshida, Phys. Rev. Lett. **70**, 525 (1993)
8. V.A. Petrov, A.V. Prokudin, Eur. Phys. J. C **23**, 135 (2002)
9. S.M. Troshin, N.E. Tyurin, Phys. Rev. D **49**, 4427 (1994)
10. S.M. Troshin, N.E. Tyurin, Eur. Phys. J. C **21**, 679 (2001)
11. P. Lebiedowicz, A. Szczurek, arXiv:1005.2309 [hep-ph]
12. V. Stoks, R. Timmermans, J.J. de Swart, Phys. Rev. C **47**, 512 (1993)
13. R.A. Arndt, I.I. Strakovsky, R.L. Workman, M.M. Pavan, Phys. Rev. C **52**, 2120 (1995)
14. ZEUS Collab., S. Chekanov et al., Nucl. Phys. B **637**, 3 (2002)
15. B.Z. Kopeliovich, B. Povh, I. Potashnikova, Z. Phys. C **73**, 125 (1996)
16. K.G. Boreskov, A.B. Kaidalov, L.A. Ponomarev, Sov. J. Nucl. Phys. **19**, 565 (1974)
17. K.G. Boreskov, A.B. Kaidalov, V.I. Lisin, E.S. Nikolaevskii, L.A. Ponomarev, Sov. J. Nucl. Phys. **15**, 203 (1972)
18. A.B. Kaidalov, V.A. Khoze, A.D. Martin, M.G. Ryskin, Eur. Phys. J. C **47**, 385 (2006)
19. B.Z. Kopeliovich, I.K. Potashnikova, Ivan Schmidt, J. Soffer, Phys. Rev. D **78**, 014031 (2008)
20. B.Z. Kopeliovich, I.K. Potashnikova, I. Schmidt, J. Soffer, AIP Conf. Proc. **1056**, 199 (2008)
21. W.J. Robertson, W.D. Walker, J.L. Davis, Phys. Rev. D **7**, 2554 (1973)
22. G.F. Chew, F.E. Low, Phys. Rev. **113**, 1640 (1959)
23. C. Goebel, Phys. Rev. Lett. **1**, 337 (1958)
24. The Compact Muon Solenoid, Technical Proposal, CERN/LHCC-94-38, LHCC/P1
25. A.S. Ayan et al., CMS-IN-2006/54
26. O.A. Grachov et al. (CMS Collaboration), J. Phys. Conf. Ser. **160**, 012059 (2009)
27. V.A. Petrov, R.A. Ryutin, A.E. Sobol, J.-P. Guillaud, arXiv:0711.1794 [hep-ph]
28. T. Sjostrand, S. Mrenna, P. Skands, J. High Energy Phys. **0605**, 026 (2006)
29. M. Albrow et al., JINST **4**, P10001 (2009)
30. D.V. Shirkov, I.L. Solovtsov, Phys. Rev. Lett. **79**, 1209 (1997)
31. S. Bethke, J. Phys. G **26**, R27 (2000)